Optical Engineering

OpticalEngineering.SPIEDigitalLibrary.org

Spectrally resolved modal characteristics of leaky-wave-coupled quantum cascade phase-locked laser arrays

Chris Sigler
Ricky Gibson
Colin Boyle
Jeremy D. Kirch
Donald Lindberg, III
Thomas Earles
Dan Botez
Luke J. Mawst
Robert Bedford

SPIE.

Chris Sigler, Ricky Gibson, Colin Boyle, Jeremy D. Kirch, Donald Lindberg, , IIIThomas Earles, Dan Botez, Luke J. Mawst, Robert Bedford, "Spectrally resolved modal characteristics of leaky-wave-coupled quantum cascade phase-locked laser arrays," *Opt. Eng.* **57**(1), 011013 (2017), doi: 10.1117/1.OE.57.1.011013.

Spectrally resolved modal characteristics of leaky-wave-coupled quantum cascade phase-locked laser arrays

Chris Sigler,[a] Ricky Gibson,[b,c] Colin Boyle,[a] Jeremy D. Kirch,[a] Donald Lindberg III,[d] Thomas Earles,[d] Dan Botez,[a] Luke J. Mawst,[a,*] and Robert Bedford[c]
[a]University of Wisconsin-Madison, Department of Electrical and Computer Engineering, Madison, Wisconsin, United States
[b]University of Dayton Research Institute, Dayton, Ohio, United States
[c]Air Force Research Laboratory, Sensors Directorate, Wright-Patterson Air Force Base, Ohio, United States
[d]Intraband, LLC, Madison, Wisconsin, United States

Abstract. The modal characteristics of nonresonant five-element phase-locked arrays of 4.7-μm emitting quantum cascade lasers (QCLs) have been studied using spectrally resolved near- and far-field measurements and correlated with results of device simulation. Devices are fabricated by a two-step metal-organic chemical vapor deposition process and operate predominantly in an in-phase array mode near threshold, although become multimode at higher drive levels. The wide spectral bandwidth of the QCL's core region is found to be a factor in promoting multispatial-mode operation at high drive levels above threshold. An optimized resonant-array design is identified to allow sole in-phase array-mode operation to high drive levels above threshold, and indicates that for phase-locked laser arrays full spatial coherence to high output powers does not require full temporal coherence. [DOI: 10.1117/1.OE.57.1.011013]

Keywords: quantum cascade lasers; MOCVD; phase-locked laser array.

Paper 170926SS received Jun. 15, 2017; accepted for publication Aug. 16, 2017; published online Sep. 19, 2017.

1 Introduction

Scaling the single-spatial-mode, output power of quantum cascade lasers (QCLs) remains an important challenge. Many applications, such as remote sensing of pollutants and explosives, require multiwatt output powers in the mid-infrared spectral region with high beam quality. Coherently combining multiple lasers monolithically in a phase-locked array configuration is an attractive approach to scale the output power, provided high beam quality can be adequately maintained. It has been theoretically shown[1] that array-element phase locking that ensures strong overall interelement coupling occurs only when each element equally couples to all others (so-called "parallel" or "global" coupling). Global coupling provides intermodal-discrimination maximization and uniform near-field intensity profiles, thus leading to immunity to the onset of high-order mode oscillation at high drive levels above threshold. Furthermore, global coupling leads to arrays that are fundamentally stable against coupling-induced instabilities,[2] in sharp contrast to nearest-neighbor or "series" coupling,[1] which is prone to self-pulsating behavior and readily causes multimode operation as the drive current increases above threshold.

A variety of techniques have been used to produce monolithic phase-locked QCL arrays that have either global coupling or series coupling. *Y*-branch coupled-ridge waveguides, which is one way to achieve global coupling, operating at $\lambda = 10.8$ μm have demonstrated pulsed in-phase mode operation from six elements, but with no increase in brightness due to modal competition.[3] By employing resonant leaky-wave coupling for phase-locking arrays of antiguides,[4] global coupling has led to 5.5 W near-diffraction-limited (DL) power from five-element arrays operating at $\lambda = 8.4$ μm. As described below, resonant leaky-wave coupling has also been employed for obtaining global coupling in THz phase-locked QCL arrays.[5,6] Global coupling has also been achieved using antenna mutual coupling for phase locking two-dimensional (2-D) surface-emitting arrays of THz DFB QCLs, up to 6.5 mW peak power at 10 K.[7] Integrated Talbot cavities have been used at the back end of phase-locked three-element[8] and six-element[9] ridge-guide laser arrays for intermodal discrimination. For the three-element array,[8] up to 375 mW were obtained in an in-phase, near-DL beam pattern, but at a serious penalty in efficiency (e.g., halving of the slope efficiency) most likely due to strong edge diffraction losses in the Talbot cavity of such low-element-number arrays. For the six-element array,[9] 4 W near-DL peak power was obtained in both the in-phase and out-of-phase array modes, as expected from theory[10] when the Talbot-cavity length is equal to one-half of the Talbot distance Z_t. However, the Talbot-cavity method does not in general employ global coupling for phase-locking, but rather a type of the nearest-neighbor coupling (diffraction coupling), thus multimode performance is expected for large-element-number arrays.[11] Shallow-etched evanescent-wave-coupled ridges with interelement gain and a small positive-index step ($\Delta n = 0.005$), operating at $\lambda = 4.6$ μm, produced a relatively wide in-phase-like beam pattern: $4.2 \times$ DL right at threshold, that further widened with increased drive, from a 700-μm wide array composed of 100 elements.[12] Such behavior is typical of evanescent-coupled arrays which, by definition, employ nearest-neighbor coupling.

*Address all correspondence to: Luke J. Mawst, E-mail: ljmawst@wisc.edu

In contrast to phase-locked laser arrays employing evanescently coupled elements, arrays of resonant leaky-wave-coupled antiguided lasers have allowed for watt-range peak pulsed and CW near-DL, in-phase-beam powers in the near-infrared.[13–16] Resonant leaky-wave coupling occurs when the interelement regions' width is equal to an integer multiple of half the projected wavelength λ_1 in the lateral direction of the leaked radiation from each element (e.g., $m\lambda_1/2$).[13] To achieve in-phase-mode resonance for linear arrays, m must be an odd integer. Such resonantly coupled devices are in fact high-index-contrast ($\Delta n = 0.08$ to 0.10) photonic crystal (PC) structures in which gain is preferentially placed in the low-index sites of the crystal,[17] and support modes that exhibit global coupling between the array elements. 2-D phase-locked arrays of surface-emitting DFB THz QCLs operating in an in-phase mode have achieved resonant leaky-wave coupling via sections at the longitudinal ends of the elements, emitting in a near-DL beam 4 mW at 20 K from a four-element array,[5] or ~1 mW at 10 K from a six-element array.[6] Since a 180-deg rotation corresponds to a π phaseshift, m must be an even integer to achieve resonance for an in-phase mode in this case.

QCLs exhibit a maximum operating-current density ($J_{\max}$), which is dependent on the injector doping level, but is typically in the range of 4 to 5× the threshold-current density, J_{th}. Thus, for a given slope efficiency, the maximum output power, under pulsed (nonheating) operation, can be scaled only by increasing the device emitting area. Longer cavity length can be used to scale the device area; although, internal losses will generally limit the practical cavity lengths which can be used without incurring a significant reduction in slope efficiency. An increase in the device-emitting width poses problems like multispatial-mode operation as well as ineffective heat removal in CW operation. The antiguided-array device concept offers a path to increase the device emitting area, while providing strong selectivity for lasing in a single spatial mode.[13] In addition, heat-spreader layers in the array can effectively thermally decouple the array elements and thus minimize thermal cross talk.[4,18] Antiguided arrays of QCLs emitting at both 8.36[4] and 4.7 μm[19] have been recently reported to operate with high beam quality to multiwatt output powers under pulsed current conditions. Resonant leaky-wave coupling of QCL phase-locked arrays was reported at $\lambda = 8.36$ μm, which resulted in in-phase-mode operation up to 5.5 W peak-pulsed power in a near-DL beam pattern.[4] Achieving resonant coupling at 4.7 μm presents further fabrication challenges because of the requirement for smaller interelement widths. Near-resonant leaky-wave-coupled QCLs emitting near 4.7 μm were recently reported,[19] which operated with up to 3.6 W peak-pulsed power with a narrow beamwidth ($\leq 1.7 \times$ DL). Those nonoptimized devices exhibit lasing predominantly in the in-phase array mode, although, lasing in a mixture of array modes is evident at high drive currents. Here, we further analyze the modal behavior of two such devices employing spectrally resolved near- and far-field measurements and their correlation to simulation. These studies help elucidate the role of the QCL spectral width on array-mode properties. A key finding is that the inherently large spectral bandwidth of this QCL's active region can promote multispatial mode operation for array designs not optimized for achieving a large intermodal-discrimination process window around the resonance condition. New, optimized resonant-array designs are presented that exhibit enhanced intermodal discrimination for achieving sole in-phase array-mode operation and thus hold potential for maintaining a DL beam pattern to high drive levels above threshold.

QCLs have been shown to exhibit very broad spectral bandwidths that widen with increasing output power.[20] The large spectral width of QCLs results from the instabilities arising from electron-light dynamics. Prior simulations of antiguided phase-locked arrays of QCLs performed in Ref. 19 considered only a single laser wavelength value located at the center of the core region's gain spectrum, while the geometrical array parameters were varied. Thus, the impact of the inherently wide spectral bandwidth of QCLs on the array-beam properties has not been previously studied. Furthermore, while spectrally resolved far-fields of a single-element THz QCL device have been measured,[21] there are no prior reports regarding the spectrally resolved near- and far-field measurements for phase-locked QCL arrays. We show that nonresonant devices can be significantly impacted by this large spectral bandwidth, leading to multimode operation with increasing drive current. Further optimized, resonantly coupled designs can be used to minimize the impact of the large spectral emission bandwidth and allow for single lateral array-mode operation to high drive levels.

2 Phase-Locked HC-PC QCL Array Structure

Two elements of the fabricated high-index-contrast, photonic crystal (HC-PC) structure are schematically shown in Fig. 1. These arrays are fabricated using a two-step metal-organic chemical vapor deposition (MOCVD) process, as described in Ref. 19. Within fabrication constraints, the interelement-region width can be adjusted to target the resonant-coupling condition. We define the interelement width as the width of the trench at the top of the upper-core region, which we call S_t, as shown in Fig. 1. The value of S_t will depend on both the trench etching to form the interelement regions as well as the thickness of the regrown layers. In the center of the core region an InP-spacer layer is placed, which acts both as a lateral heat remover[18] as well as the base layer for the regrowth of the interelement regions. The structure design optimization approach for achieving single lateral-mode operation has been addressed previously;[22] although, that previous analysis assumed single-wavelength emission. The regrown interelement regions have $In_{0.53}Ga_{0.47}As$ layers and lowered Ti/Pt/Au regions that create a higher effective refractive index than in the element regions, as well as strong interelement losses due to plasmon coupling to the metal (as schematically shown in Fig. 1). As a result, an array of antiguides of large index step ($\Delta n > 0.05$) is formed, which can be designed to strongly favor in-phase array-mode operation. In the context of the effective-index approximation, resonant leaky-wave coupling occurs when the interelement regions' width is equal to an integer multiple of half the laterally projected wavelength, $\lambda_1 = \lambda/\sqrt{n_1^2 - n_{\text{eff}}^2}$, in the lateral direction,[13,23,24] where n_1 is the transverse effective index in the interelement region, and n_{eff} is the array-mode effective index. For actual 2-D waveguide structures, the resonance point is shifted due to significantly low overlap between the fields of the fundamental transverse modes in the element and interelement regions.[13,25] Thus, full-wave modeling, such as using COMSOL Multiphysics, is necessary to

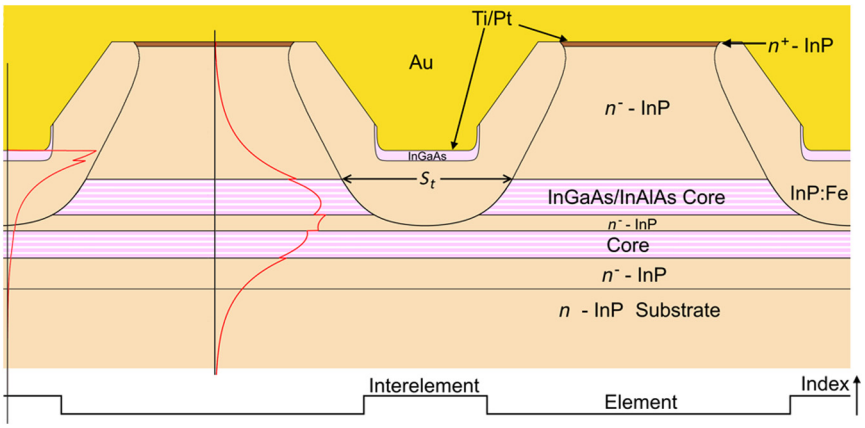

Fig. 1 Schematic representation of the cross-sectional view of HC-PC QCL structure under study.

analyze the array structure to find the actual resonance condition where the photonic bandgap is zero.[17,19] For a given emission wavelength, resonance is generally achieved by varying the array-interelement width on the photomask and fixing the regrown-layer thicknesses to target the desired lateral index step, as was done in this work where we present results from two arrays of different interelement width. Achieving the resonance condition leads to parallel/global coupling among all array elements and nearly uniform near-field intensity profiles for the array resonant modes.[23,24] Here, the desired resonant mode is composed of fundamental element modes coupled in-phase and with an interelement spacing $S_t \sim \lambda_1/2$.[13] As discussed below, for the devices described here, the resonance condition was not met as a result of too large an interelement spacing. Generally, an iterative fabrication process is used to experimentally achieve resonant devices.

A 35-stage core region with a 0.5-μm thick InP spacer layer was grown by MOCVD using a core-region structure similar to that of state of the art 4.6 to 4.7 μm emitting QCLs.[26] The fabrication process follows that of Ref. 19. Three millimeters long, high-reflectivity-coated chips were tested under pulsed operation in the epi-side up configuration. The devices were not tested in CW or quasi-CW operation, which would require epi-side down mounting and electroplating thick gold onto the epi-side to improve the devices' thermal conductance and planarity (to reduce voids at the bond-line above the interelements). Cross-sectional scanning electron microscope images at the emitting facet of one of the fabricated devices are shown in Fig. 2.

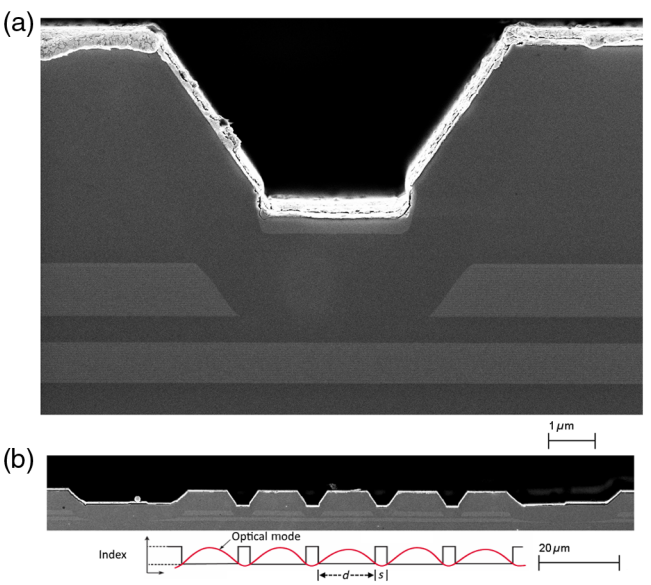

Fig. 2 SEM images of the fabricated five-element array: (a) interelement region, (b) complete five-element device with a schematic of the effective-index structure and in-phase mode profile.

3 Experimental Results

Figure 3 shows the light-current (L-I) curves of two five-element arrays with interelement widths of 5.3 and 6.0 μm, in pulsed operation (200 ns-wide pulses, 20 kHz repetition rate). The element widths are nominally the same for the two devices, resulting in slightly different total widths for the arrays: ~80 and ~83 μm at the top of the upper core. The threshold currents are ~4.7 A which corresponds to a threshold current density, J_{th}, value of ~1.7 kA/cm^2 in the lower core when considering current spreading under the interelement regions and 5 μm into each of the two lower corners of the core at the array edges. The peak powers of the devices reached are 4.5 and 5.8 W for the narrow and wide interelement devices, respectively. Higher output power is observed from the device with wider interelement

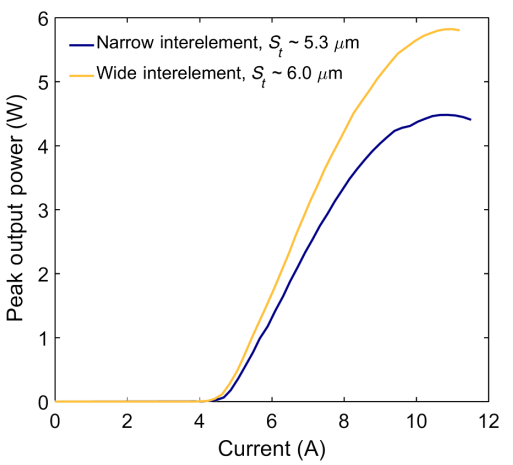

Fig. 3 Measured L-I characteristics under pulsed operation for two arrays of different interelement spacings.

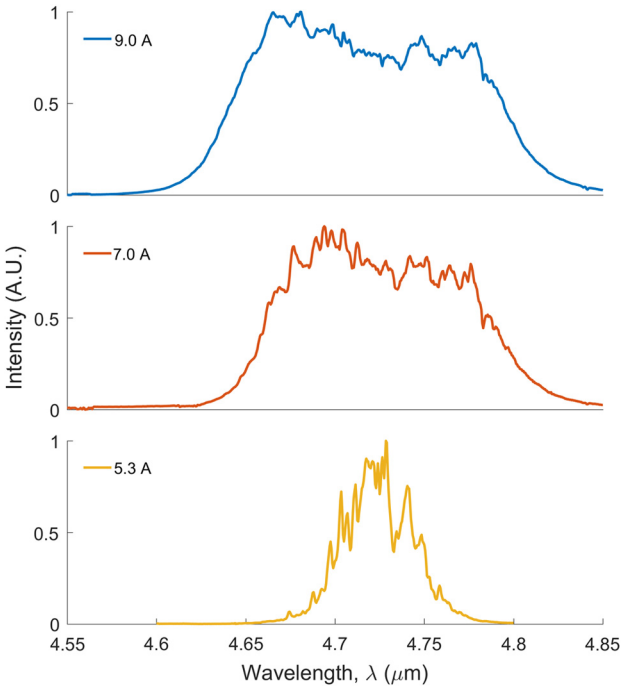

Fig. 4 Measured spectrum under different drive currents for the array with wide interelement spacing ($S_t \sim 6.0$ μm).

width, since modal losses are reduced for designs that are further from the resonance condition.[19]

The measured spectra for one device ($S_t \sim 6.0$ μm) are shown in Fig. 4 under different drive currents. The spectral characteristics were measured using a HORIBA 1250-mm long spectrometer and a liquid nitrogen-cooled InSb detector, with a ~3-nm spectral resolution. The beam was focused on the entrance slit of the spectrometer using a spherical lens to collect light within a divergence half-angle of ~16 deg.

3.1 *Near-Field Measurements*

3.1.1 *Setup*

Initially the full spectral band near-field is directly imaged. The output facet of the QCL is imaged using a 0.85 numerical aperture GeSbSe antireflective-coated infrared asphere (effective focal length = 1.87 mm, working distance = 0.72 mm) directly onto an InSb 640×512 pixel focal plane array (FPA) cooled to 76 K with a pixel pitch of 15 μm. The optical system results in a magnification of ~85 and a spatial sampling of just under 180 nm. Images are collected using a 0.96 μs exposure time triggered by the pulsed repetition frequency (PRF, 1kHz to prevent detector saturation) of the pulsed current source and are averaged over 2500 frames, and corrected to remove the background. This approach typically results in near-field images utilizing 10 bits of the 14-bit sampling.

To spectrally resolve the near-field, we use a similar setup as for the full-spectrum above, but instead of imaging onto an FPA, we image the near-field onto 100-μm wide entrance slits of a 300-mm long spectrometer with a 300 line/mm grating. To attain reasonable near-field resolution, we adjust the setup to attain a magnification of ≈210. The exit slits of the spectrometer are set equal to the entrance slits and an amplified single-channel PbSe detector and lock-in amplifier, with a time constant of 300 ms, are used to measure the spectrally resolved signal. The spectral resolution is estimated to be <5.2 nm. To build up a transverse near-field profile, the imaging lens is translated horizontally, thus translating the near-field image across the entrance slits. The imaging lens translation step size is chosen to correspond to a 1-μm spatial sampling on the QCL facet (object space). The devices are operated with a pulse width of 200 ns, at a submount temperature of 20°C, and a PRF of 10 to 20 kHz, depending on the device and detector saturation. We did ensure that there is no significant performance difference between 1 and 20 kHz, such that the duty cycle was appreciably small and there was little pulse-to-pulse thermal "memory."

3.1.2 *Analysis*

Line scans of full spectral band near-field images are from the center height of the image and the average of three detector rows. There is a slight asymmetry in the near-field, which is likely due to fabrication nonuniformity. Figure 5 shows the near-field images for operation near threshold, showing good agreement between the near-field summed over all spectral bands and the near-field profile directly imaged with the

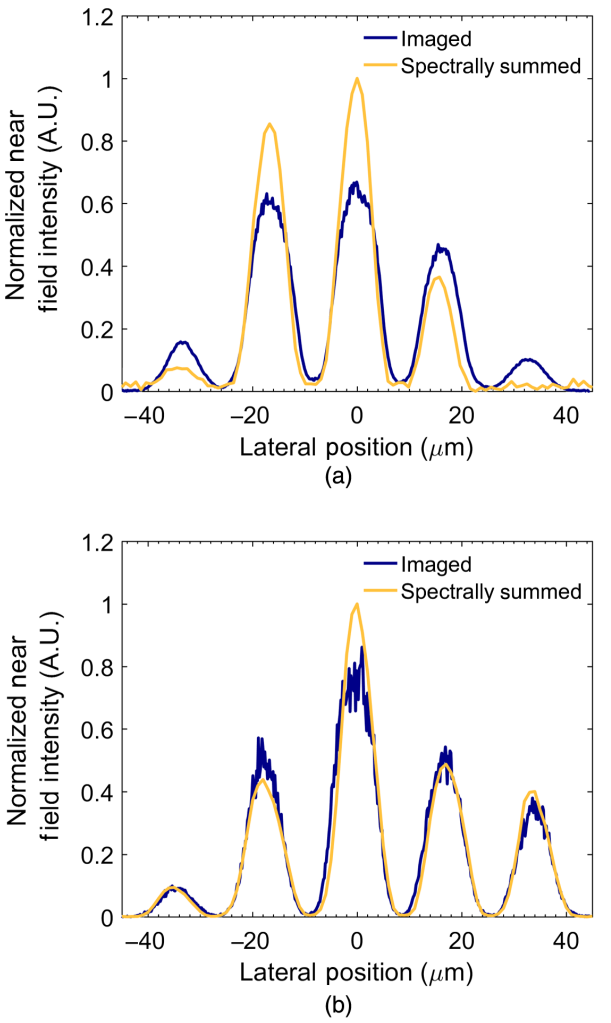

Fig. 5 Comparison of near-field profiles directly imaged and summed from the spectrally resolved imaging for the (a) narrow interelement device and (b) wide interelement device.

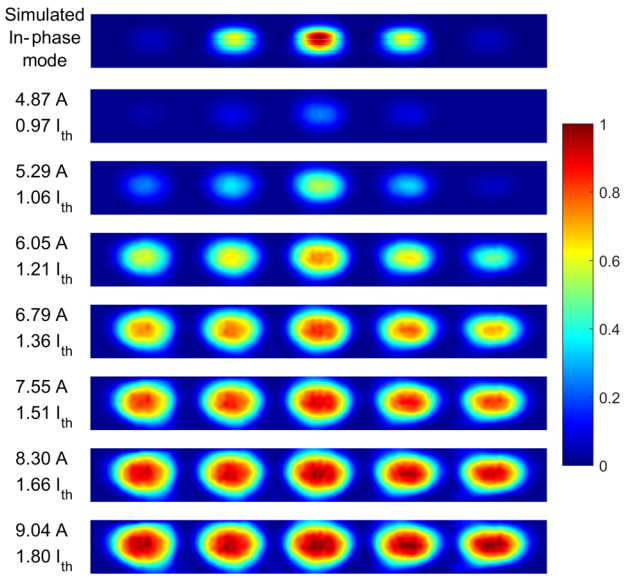

Fig. 6 Measured full spectrum near-field profile of the wide interelement device as a function of current (bottom); simulated in-phase mode near-field intensity profile for this device geometry (top).

InSb FPA. The narrow interelement device [Fig. 5(a)] contains strongly peaked central lobes relative to the outer two lobes. The two measurements in Fig. 5(a) are taken at slightly different current drives, with the directly imaged measurement at 0.1 A higher drive, resulting in some difference between the directly imaged near-field and a summation of the spectrally resolved near-field. In addition, low signal data points in the outer lobes are in the noise floor for certain wavelengths, thus they do not contribute to the spectral sum. In contrast, Fig. 5(b) shows the wide interelement device where there is a little more power in the outer two lobes relative to the inside three lobes, and the two curves agree well with each other as the measurements were taken at the same current.

Figure 6 shows the full spectral band near-field profile as a function of current for the wide interelement device, as well as the simulated in-phase mode profile for this device. Simulations show the in-phase mode of these devices was highly nonuniform and peaked in the center element of the array. This suggests that the in-phase mode lases first near threshold for this device, and as the drive current increases other modes with more intensity in the outer elements begin to lase and fill in the near-field to give a nearly uniform intensity profile.

3.2 *Far-Field Measurements*

3.2.1 *Setup*

To measure the far-field beam patterns of the devices including the full spectral band, the device is placed on a rotational stage centered at the output facet, 40 cm away from a liquid nitrogen-cooled InSb detector with a 25-μm wide vertical slit placed in front of it, giving each individual measurement an angular resolution of 0.007 deg. Two hundred nanoseconds long current pulses with a repetition rate of 20 kHz are used and a boxcar integrator converts the power pulse into a single data point. The rotational mount is rotated and a data point is taken approximately every 0.25 deg.

In contrast with Ref. 21, where a microbolometer FPA was used in conjunction with an FTIR spectrometer to capture the spectrally resolved far-field in parallel, we measure the spectrally resolved far-field with a single pixel detector, which in general should increase the measurement time and improve the signal-to-noise ratio of the measurement. The device is placed 18 cm away from the 1-mm wide entrance slit of a HORIBA 1250-mm long spectrometer with a 300 line/mm grating. A cylindrical lens is used to focus the vertical axis of the beam onto the entrance slit of the spectrometer. A liquid nitrogen-cooled InSb detector is used with a lock-in amplifier with 300 ms time constant to record the spectrum of the device for a given angle. The device is rotated to obtain different slices of the far-field passing through the entrance slit to build the full spectrally resolved beam pattern. The estimated angular and spectral resolutions of this system are 0.32 deg and 3 nm, respectively.

3.2.2 *Analysis*

Full spectrum far-fields as a function of current are shown for the two devices in Fig. 7, along with the simulated in-phase

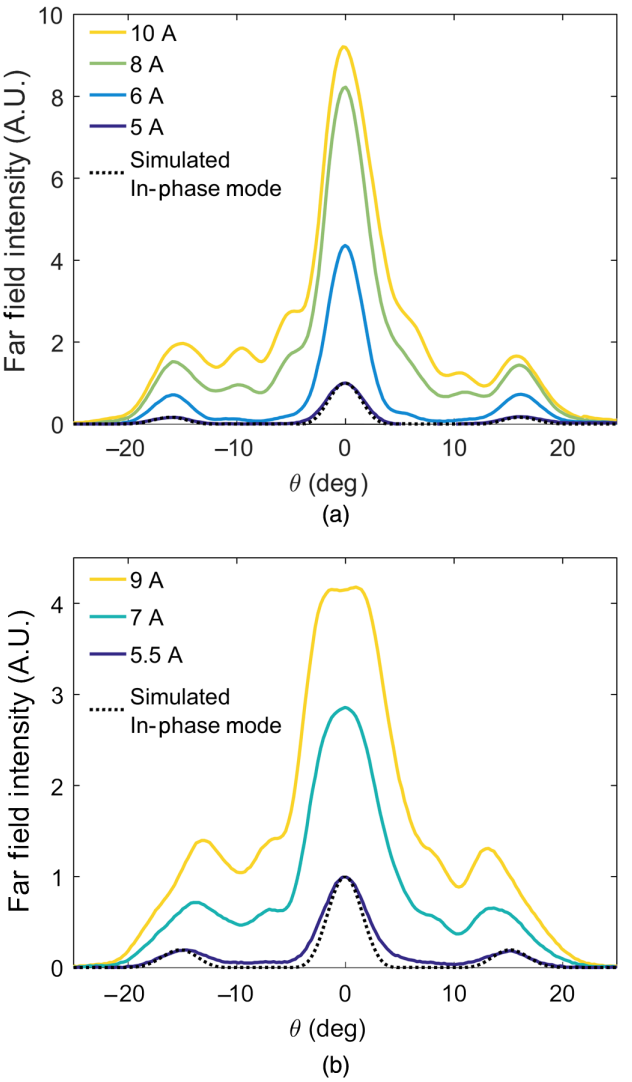

Fig. 7 Measured (upper) and simulated (lowest) lateral far-field patterns for HC-PC device with an interelement width of (a) 5.3 μm and (b) 6.0 μm.

mode, which is the ideal DL beam pattern. These indicate operation near threshold primarily in the in-phase array mode, with central lobe full-widths at half-maximum (FWHM) of $1.1 \times$ DL. and $1.3 \times$ DL, for the narrow and wide interelement devices, respectively. The sidelobe intensities near threshold are in agreement with the simulation to within the noise of the measurement for the narrow interelement device, and up to 6% lower intensity than the simulation for the wide interelement device. The beams broaden at higher drive currents due to the onset of adjacent modes reaching threshold.[13,27] For the device of smaller interelement width ($S_t \sim 5.3$ μm) with an ~80-μm wide aperture,

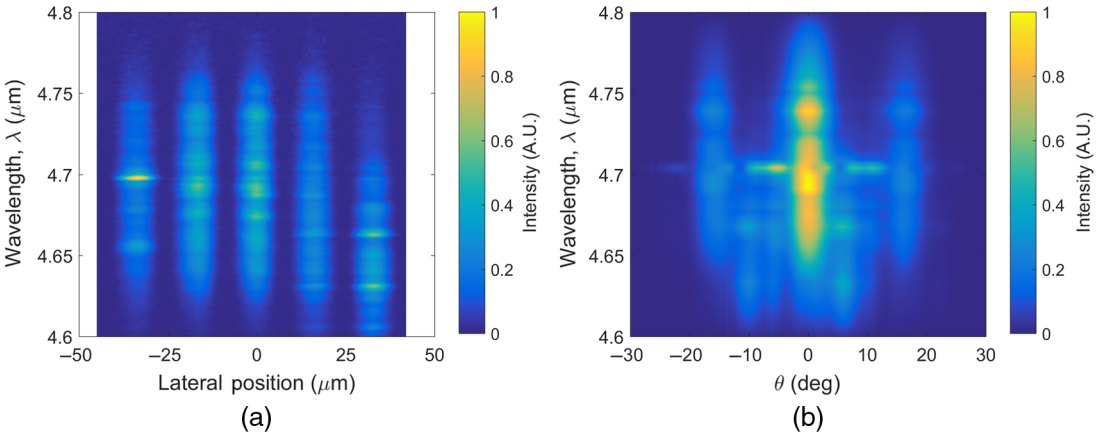

Fig. 8 Contour plots of the spectrally resolved (a) near-field and (b) far-field profiles for the narrow interelement device at a current drive near rollover (9.2 A).

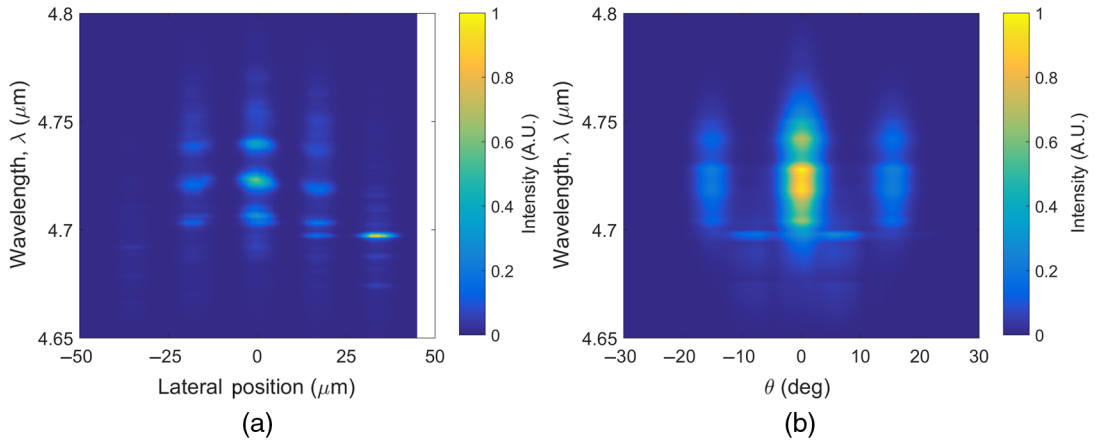

Fig. 9 Contour plots of the spectrally resolved (a) near-field and (b) far-field profiles for the wide interelement device at a current drive near threshold (5.3 A).

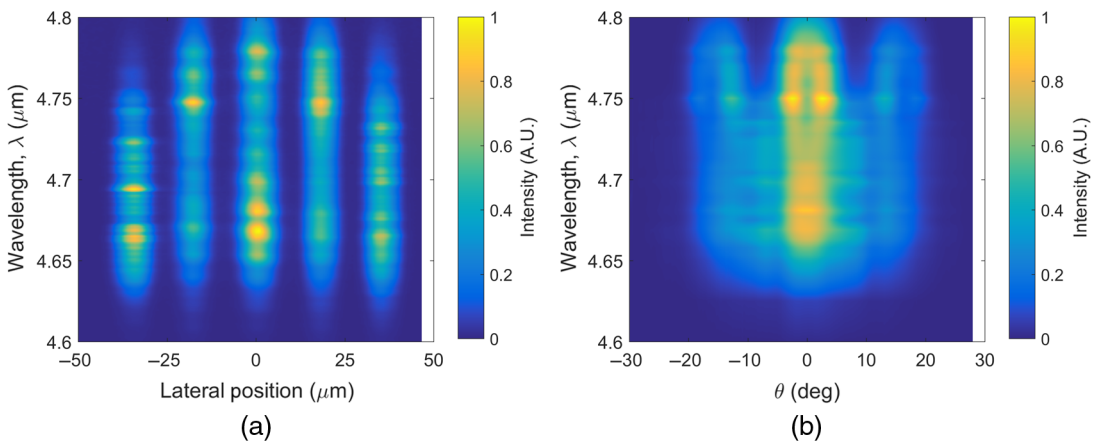

Fig. 10 Contour plots of the spectrally resolved (a) near-field and (b) far-field profiles for the wide interelement device at a current drive near rollover (9.0 A).

the central lobe FWHM is $1.7 \times$ DL at 10.0 A and 4.3 W output power. That is, it has near-DL operation to a drive level of 2.1× threshold [Fig. 7(a)]. For the device of larger interelement width ($S_t \sim 6.0$ μm), the beam broadens more with increasing current [Fig. 7(b)], with a lobewidth $\sim 2.6 \times$ DL at 9.0 A and a peak power of 5.1 W, indicating that above threshold lasing occurs in a much larger mixture of additional array modes. In the direction perpendicular to the

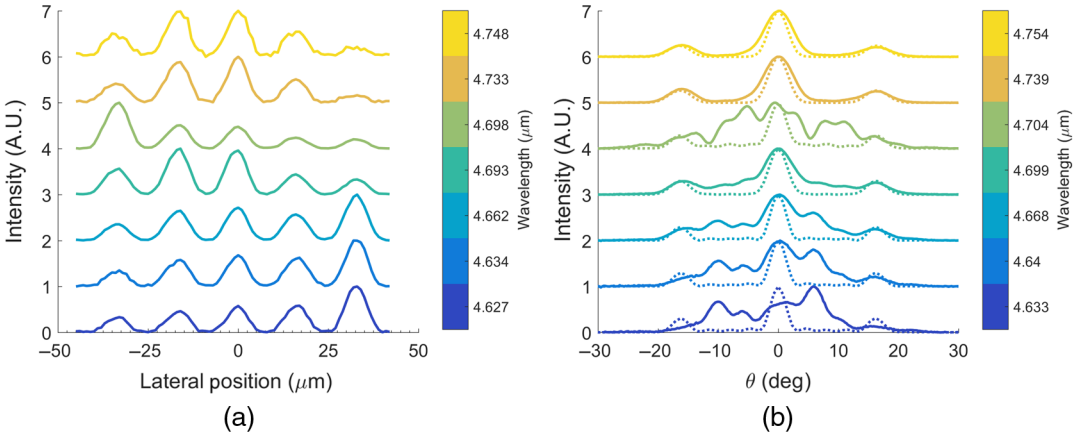

Fig. 11 Line scans at selected wavelengths of the measured spectrally resolved (a) near-field and (b) far-field profiles (solid lines) for the narrow interelement device at a current drive near rollover (9.2 A). The dotted lines in (b) are FFTs of the measured near-field profile.

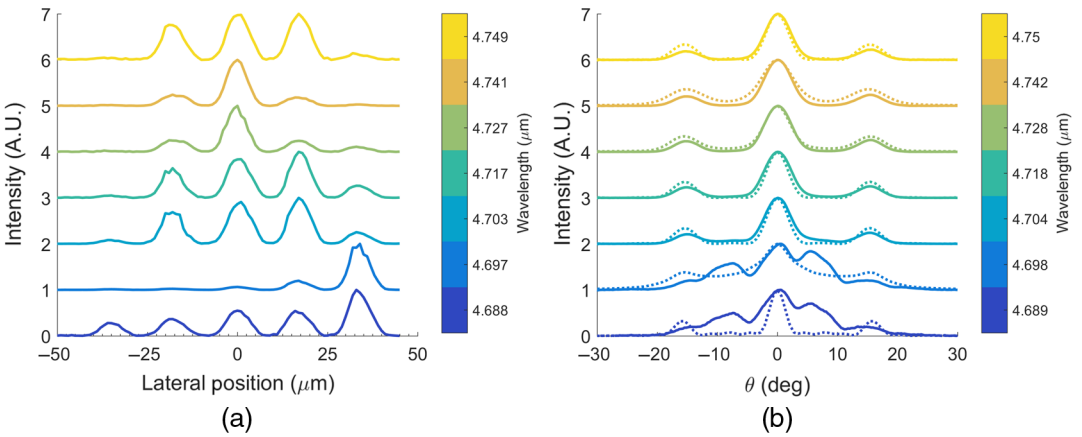

Fig. 12 Line scans at selected wavelengths of the measured spectrally resolved (a) near-field and (b) far-field profiles (solid lines) for the wide interelement device at a current drive near threshold (5.3 A). The dotted lines in (b) are FFTs of the measured near-field profile.

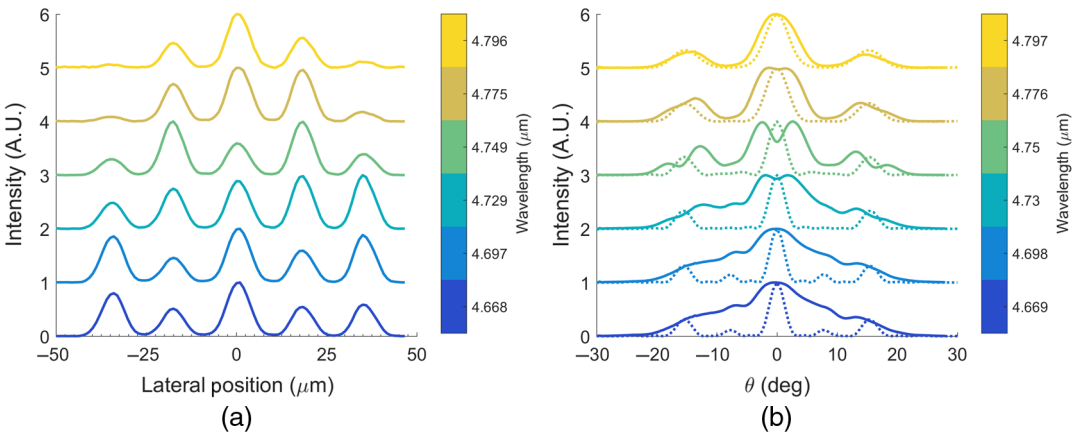

Fig. 13 Line scans at selected wavelengths of the measured spectrally resolved (a) near-field and (b) far-field profiles (solid lines) for the wide interelement device at a current drive near rollover (9.0 A). The dotted lines in (b) are FFTs of the measured near-field profile.

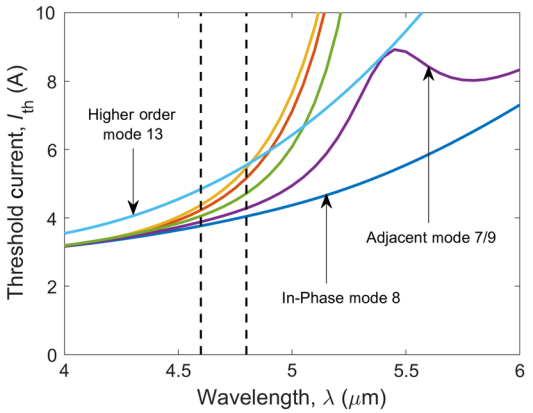

Fig. 14 Simulated threshold currents for selected modes supported by the narrow interelement ($S_t \sim 5.3$ μm) five-element HC-PC device as a function of wavelength. The dotted black lines represent the approximate wavelength bounds within which these devices lased.

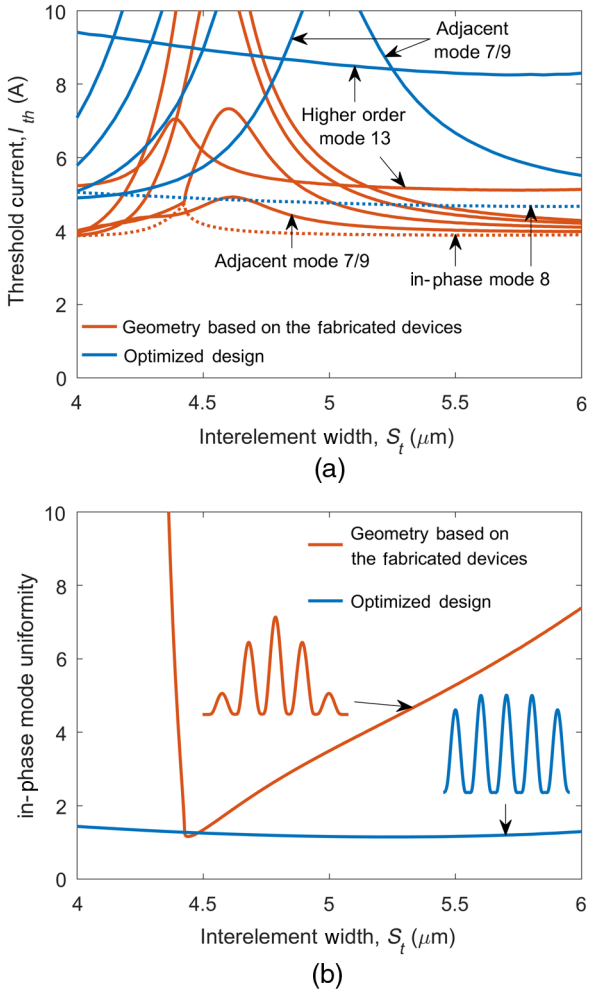

Fig. 15 (a) Simulated threshold currents for selected modes supported by five-element HC-PC devices as a function of interelement width, S_t, at the design wavelength of 4.7 μm, using both a geometry based on the fabricated devices and an optimized design. The dotted lines are the in-phase modes for each structure. (b) Simulated in-phase mode uniformity, for the same two structures. The insets show the lateral in-phase mode intensity profile at an interelement width 0.7 μm away from resonance for each structure.

array, the measured far-field has an FWHM of 45 deg, compared to a calculated FWHM of 43 deg for the fundamental transverse element mode, suggesting they are DL in that direction.

In these leaky-wave-coupled arrays, the near- and far-field distributions are found to be wavelength dependent. Figures 8–10 show contour plots of the measured spectrally resolved near and far-fields for the narrow interelement device near rollover, wide interelement device near threshold, and wide interelement device near rollover, respectively. Figures 11–13 show selected line scans of the spectrally resolved near and far-fields of the devices in the same order. Spectrally resolved far-fields of the narrow interelement device were measured near threshold, at 5.9 A, and showed little deviation from the expected in-phase mode far-field at all measured wavelengths. Due to the near-field and far-field measurements being taken with different systems and variations in the measured spectra for a given device over time, the near-field and far-field measurements at a specific wavelength are not necessarily comparable. Thus, we measure the spectrum for a given device and drive level between the two systems and find an offset between corresponding peaks in

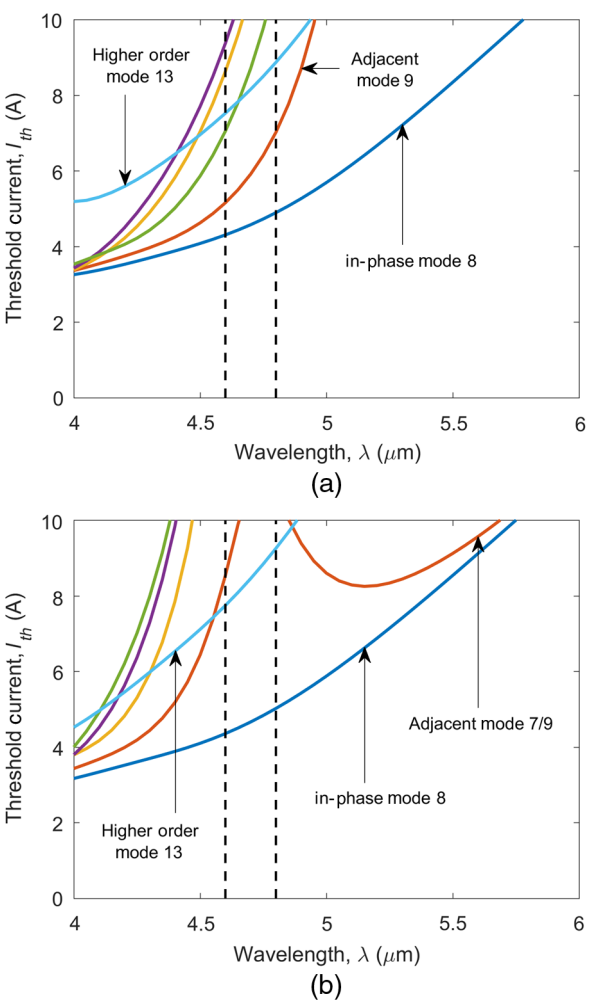

Fig. 16 Simulated threshold currents for selected modes supported by the optimized HC-PC design as a function of wavelength, at an S_t value of: (a) 5.7 μm and (b) 5.0 μm, the resonance condition. The dotted black lines represent the approximate wavelength bounds within which the fabricated devices lased.

the spectra, which ranged up to 6 nm. We then compare the near and far-fields at two wavelengths separated by that offset. Both the near- and far-field measurements are background- and detectivity-corrected.

Fourier transforms of the near-field imaging from image space (emission plane) to angular space are used to compare the near-field imaging to the far-field imaging. The square root of near-field intensity is zero-padded such that the "padded" data are four times larger than the original data. This results in an angular resolution of 0.73 deg for the transforms of the spectrally resolved near-field profile. In all cases, the angular resolution is comparable to the experimental resolution. The square of the Fourier transform is normalized to the maximum value for comparison with the far-field imaging intensity. In this approach, we assume a uniform planar phasefront at the output facet, essentially true for a device operating in the ideal in-phase mode. The dotted lines in Figs. 11–13 show these Fourier-transformed near-fields and allow a comparison with the measured spectrally resolved far-fields. We can see in the spectrally resolved near-field images that at shorter wavelengths (e.g., 4.65 μm), more energy is found in the outer elements, and the far-field beam pattern is significantly different from that expected for a flat phase front, indicating operation in nonresonant modes. At longer wavelengths (≈4.75 μm), the mode is primarily confined in the central lobes and the far-field is in-phase-like for the narrow interelement device, indicating operation primarily in the in-phase mode. Figures 12(b) and 13(b) show the wide interelement device is operating with a nearly flat phase front near threshold at most wavelengths, and a more complex profile at high power. At some wavelengths, we see significantly asymmetric near-field profiles, and the corresponding far-field profiles have poor beam quality. We attribute the asymmetry to fabrication nonuniformities.

4 Modeling and Discussion

To understand the modal characteristics of these devices, simulations of these five-element array structures were performed using COMSOL Multiphysics to find the expected threshold currents and electric field profiles for the modes supported by the structures. The models' geometries were created based on SEM images of the cross-section at the emitting facet of the devices, such as those shown in Fig. 2. Expected threshold currents are calculated based on the modal loss and field profile calculated by COMSOL, as discussed in Ref. 19. The models are set up such that each

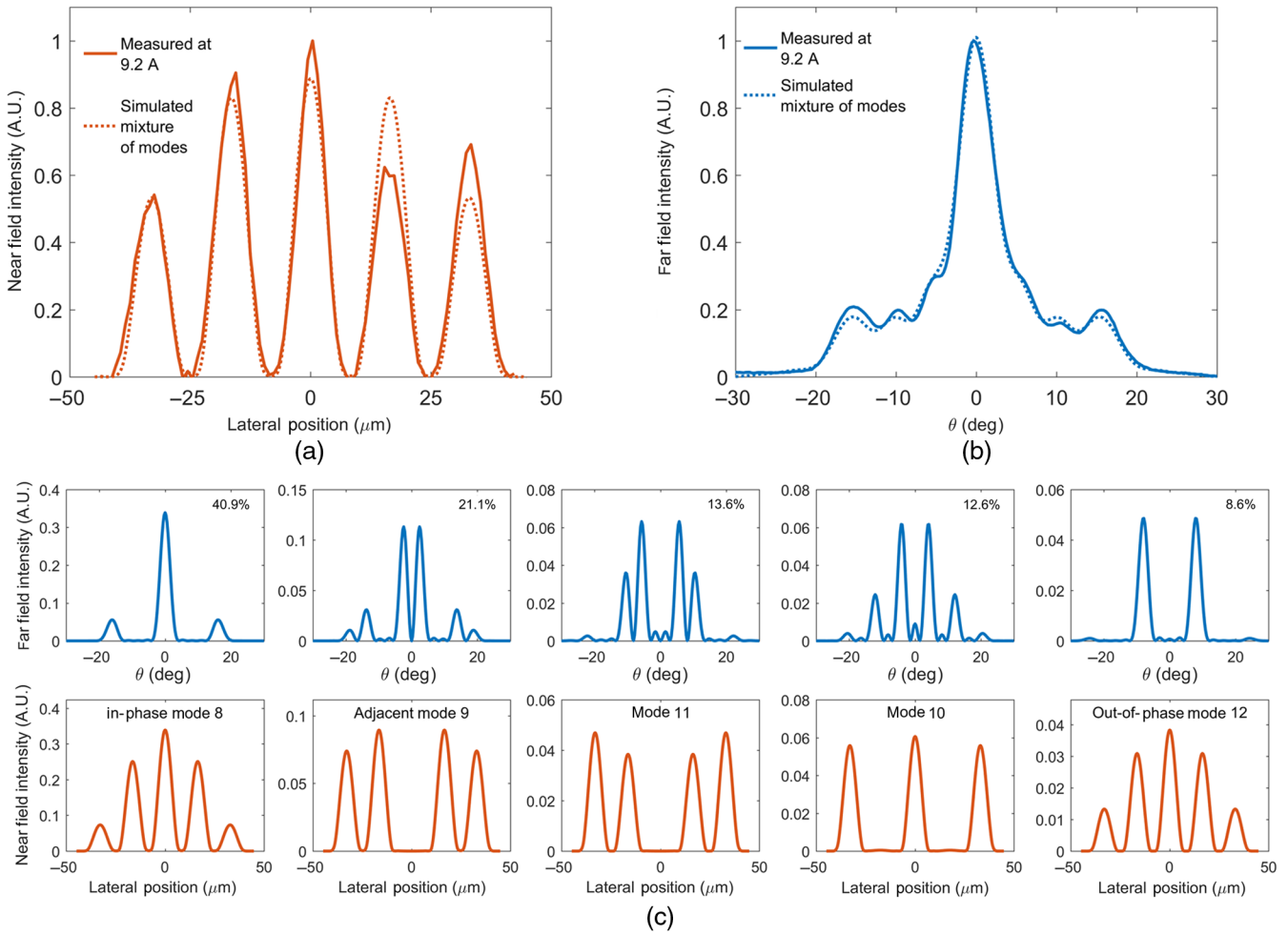

Fig. 17 Modal decomposition of the measured full spectral-band near and far-field patterns for the narrow interelement device near rollover (9.2 A): (a) comparison of the measured near-field profile to a simulated mixture of modes; (b) comparison of the measured far-field beam pattern to a simulated mixture of modes; (c) near- and far-field profiles of the modes contributing to the mixture in (a) and (b), and their relative contributions to the mixture in the top-right corner of the far-field plots.

interelement is identical and symmetric. Thus, the model produces only symmetric and antisymmetric mode profiles, and so the asymmetric near-field profiles seen in the measurements are not found.

When the interelement width, S_t, of an array approaches the width required to produce resonance, the nonresonant-array modes experience enhanced field overlap with the lossy Ti metal in the interelement regions.[13,27] Thus, they are strongly suppressed in structures with high interelement loss.[23,24,27,28] The metal-related interelement loss can be introduced with little effect on the resonant in-phase mode, due to its having little intensity in the interelement regions.[27] This creates large intermodal discrimination around resonance. As the interelement width needed to achieve resonance is proportional to the wavelength,[13] the resonance point shifts across the spectrum of the QCLs. Simulations suggest the resonance point at the design wavelength of 4.7 μm was approximately $S_t \sim 4.6$ μm. Since both these devices had interelement widths larger than that at resonance, at longer wavelengths the resonance point shifts closer to their interelement widths, thus improving intermodal discrimination at longer wavelengths. Figure 14 shows an example of this for the narrow interelement device ($S_t \sim 5.3$ μm). This figure plots the simulated threshold currents for selected competing array modes as a function of the emitting wavelength (high threshold modes have been removed for clarity). The mode numbers correspond to the number of field-intensity minima across the array for a given mode, which can change on either side of resonance for a given mode. For example, the in-phase mode is referred to as mode 8 because it has minima at either side of the four interelement regions.[13] Since the device is significantly far from resonance, this change in intermodal discrimination across wavelength is not large enough to bring the array into resonance within the core-region's spectral band. However, as seen in Fig. 11, the far-field beam profile is improved at longer wavelengths, in agreement with there being enhanced intermodal discrimination at these wavelengths. As the wavelength increases, absorption losses for the materials increase and the modes are less confined to the core, resulting in the increasing threshold with wavelength for all modes. This simulation assumes a constant differential gain coefficient regardless of wavelength.

The fabricated devices have suboptimal structures, leading to a narrow window for single-lateral-mode operation. A more optimized design, primarily consisting of removing the

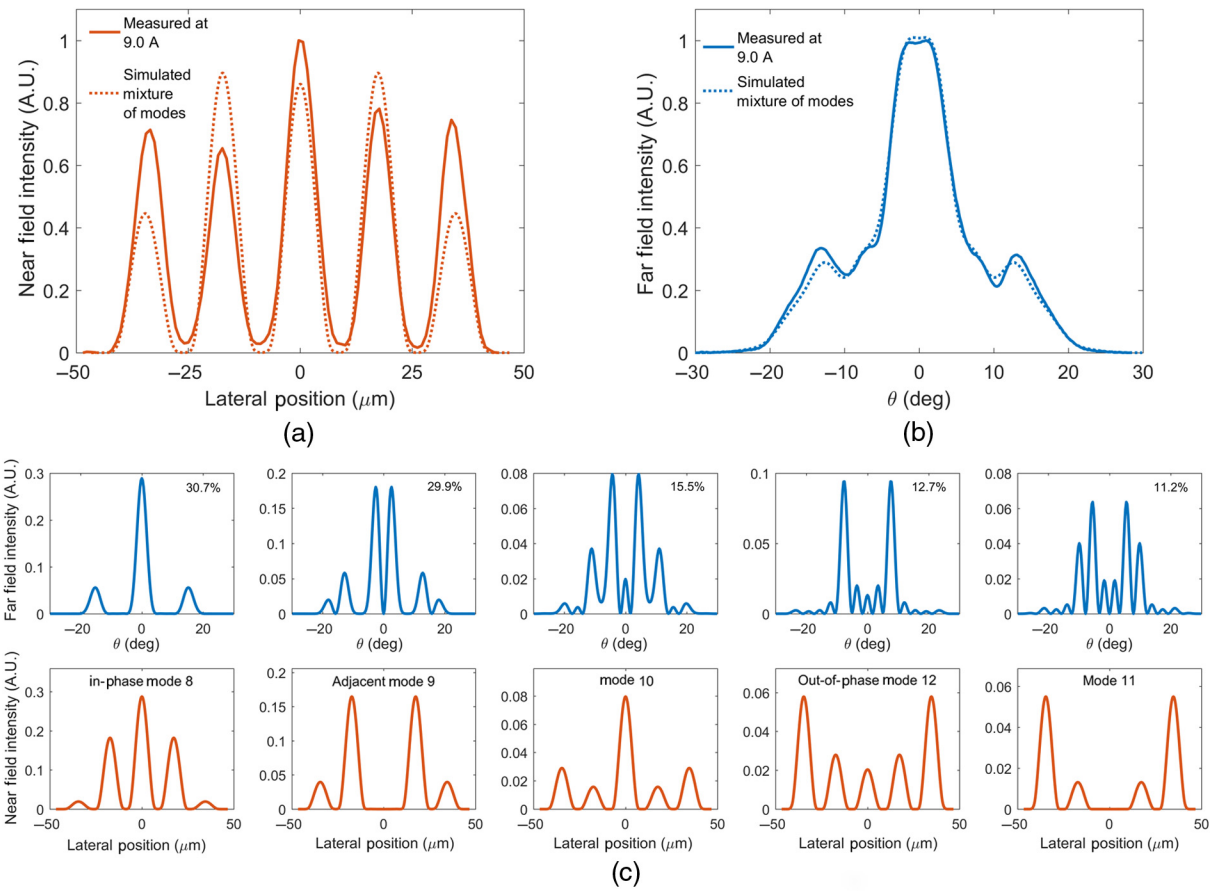

Fig. 18 Modal decomposition of the measured full spectral-band near- and far-field patterns for the wide interelement device near rollover (9.0 A): (a) comparison of the measured near-field profile to a simulated mixture of modes; (b) comparison of the measured far-field beam pattern to a simulated mixture of modes; (c) near- and far-field profiles of the modes contributing to the mixture in (a) and (b), and their relative contributions to the mixture in the top-right corner of the far-field plots.

Pt layer from the frontside metallization, narrowing the elements (10 μm instead of 12-μm wide), and widening the regrown InGaAs layer by growing thinner InP:Fe, can broaden the window for large intermodal discrimination. Figure 15(a) shows an example of simulated threshold currents versus interelement width for geometries based on that of the fabricated devices as well as for an optimized design. This simulation shows that the intermodal discrimination is larger for the narrow interelement device than for the wide interelement device, leading to the broader beam pattern for the wide interelement device. The window for single-lateral-mode operation for the optimized design is large: there is a ~0.85-μm wide region in S_t variation in which the competing modes have a threshold over 40% higher than the in-phase mode, though the in-phase mode does have a higher threshold compared to the simulation based on the fabricated devices.

Figure 15(b) shows, for the same two structures, the simulated in-phase mode uniformity, which we define as the ratio of the integral of the electric field intensity in the central element to that in an element at an edge of the array, as a function of interelement width. The insets show the lateral in-phase mode intensity profile at an interelement width 0.7 μm above resonance for both structures, which is the width obtained for the narrow interelement device. The more uniform profile of the optimized design will help reduce gain spatial hole burning at the array level, regardless of the obtained interelement width. Thus, the in-phase mode can more efficiently utilize gain, reducing the gain available to other modes to achieve lasing. A uniform near-field profile also reduces the beam width of the central lobe of the far-field, though it does increase the intensity of the side lobes.

Because of the lower doping of the InP substrate ($\sim 2 \times 10^{17}$ cm^{-3}) compared to the highly doped contact layer on the frontside ($\sim 2 \times 10^{19}$ cm^{-3}), the backside contact requires annealing to improve the resistance of this contact. This can allow Au to diffuse into the device on the frontside if a blocking metal layer, such as Pt, is not used. Thus, this design requires that the backside contact be annealed before the metal on the frontside has been deposited to avoid Au diffusion.

Figure 16 shows the simulated threshold current as a function of wavelength for this optimized design, (a) near resonance with $S_t = 5.7$ μm and (b) at resonance, for $\lambda = 4.7$ μm, with $S_t = 5.0$ μm. Figure 16(a) is at the same interelement width offset from resonance as the fabricated narrow interelement device, showing that this far from resonance there is significantly larger intermodal discrimination in comparison to the fabricated device's case shown in Fig. 14, and there is significant wavelength dependence within the device's spectral band. Figure 16(b) shows that an optimized device operating at resonance at its design

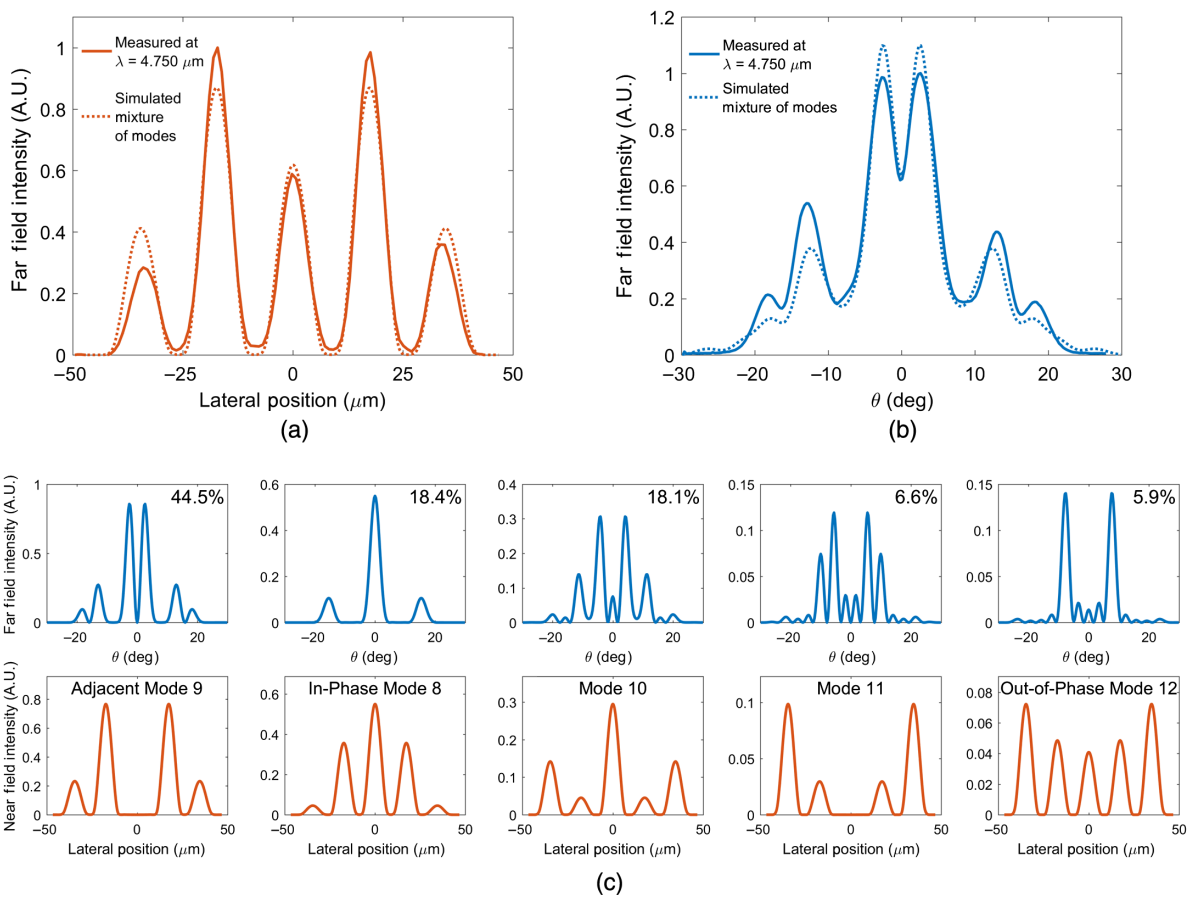

Fig. 19 Modal decomposition of the measured near- and far-field patterns for the wide interelement device near rollover (9.0 A), at a wavelength of 4.75 μm: (a) comparison of the measured near-field profile to a simulated mixture of modes; (b) comparison of the measured far-field beam pattern to a simulated mixture of modes; (c) near- and far-field profiles of the modes contributing to the mixture in (a) and (b), and their relative contributions to the mixture in the top-right corner of the far-field plots.

wavelength should exhibit single in-phase mode operation across its full spectral band. That is, as expected, achieving full spatial coherence from a phase-locked laser array does not require full temporal coherence (i.e., single-frequency operation).

The simulated near- and far-field profiles were numerically fit to the measured near- and far-field profiles to determine the modal composition of the emitted beam. This was accomplished by finding the combination of contributions from modes solved by COMSOL which minimizes the total error between the simulated and measured profiles. Figures 17 and 18 show the result of this fitting for the overall far-field beam patterns of the narrow and wide interelement devices, respectively, near rollover. For the narrow interelement device the measurements were made at 9.2 A, and for the wide interelement device the measurements were made at 9.0 A. This fitting assumes that the mode profiles are calculated at a wavelength of 4.7 μm, ignoring the variation across the spectrum. This fitting shows our best estimate of the relative contribution of the in-phase mode to the overall beam patterns for the two devices, with the narrow interelement device having greater contribution from this mode, as would be expected since it is closer to resonance. For both devices, the calculated relative contributions of the in-phase mode are larger at lower current drives: 65.5% at 5.5 A for the wide interelement device, and 87.6% at 5.0 A for the narrow interelement device. Only the competing array modes composed of coupled fundamental element modes are necessary to fit these measurements. That is, this indicates that no array modes composed of coupled first-order element modes are lasing in these devices.

Figure 19 shows fitting of near- and far-field patterns for the wide interelement device at high drive current, specifically at a wavelength of 4.75 μm, showing predominantly adjacent mode 9 lasing at this wavelength, which is the primary reason for the broadening of this overall beam.

5 Conclusions

Spectrally resolved near- and far-field measurements were taken of five-element HC-PC QCL devices. Near threshold the devices operate predominantly in an in-phase mode, and with increasing drive above threshold significantly more power originates from lasing of competing array modes. The near- and far-field beam patterns vary across the spectra of the devices. Analysis indicates the in-phase mode is favored to lase for these devices, with little intermodal discrimination, as they are nonresonant. The simulated competing array modes composed of coupled fundamental modes can be used to fit the measured near- and far-field beam patterns, indicating that no array modes composed of higher order element modes are lasing. An optimized design is shown to provide large intermodal discrimination for sole in-phase mode operation across the full spectrum of the QCL core-region material, supporting the fact that a phase-locked laser array can operate with full spatial coherence in the absence of full temporal coherence.

Acknowledgments

This work was supported in part by Air Force Research Laboratory under Grant FA8650-13-2-1616 and by Navy NAWC-CLKE under STTR Grant N68335-15-C-0073. This work was performed using facilities that were supported in part by the University of Wisconsin Materials Research Science and Engineering Center (DMR-1121288). The authors have no relevant financial interests in the paper and no other potential conflicts of interest to disclose.

References

1. W. J. Fader and G. E. Palma, "Normal modes of N coupled lasers," *Opt. Lett.* **10**(8), 381–383 (1985).
2. R. Li and T. Erneux, "Stability conditions for coupled lasers: series coupling versus parallel coupling," *Opt. Commun.* **99**(3–4), 196–200 (1993).
3. L. K. Hoffmann et al., "Tree array quantum cascade laser," *Opt. Express* **17**(2), 649–657 (2009).
4. J. D. Kirch et al., "5.5 W near-diffraction-limited power from resonant leaky-wave coupled phase-locked arrays of quantum cascade lasers," *Appl. Phys. Lett.* **106**(6), 061113 (2015).
5. Y. Halioua et al., "Phase-locked arrays of surface-emitting graded-photonic-heterostructure terahertz semiconductor lasers," *Opt. Express* **23**(5), 6915 (2015).
6. T.-Y. Kao, Q. Hu, and J. L. Reno, "Phase-locked arrays of surface-emitting terahertz quantum-cascade lasers," *Appl. Phys. Lett.* **96**(10), 101106 (2010).
7. T.-Y. Kao, J. L. Reno, and Q. Hu, "Phase-locked laser arrays through global antenna mutual coupling," *Nat. Photonics* **10**(8), 541–546 (2016).
8. L. Wang et al., "Phase-locked array of quantum cascade lasers with an integrated Talbot cavity," *Opt. Express* **24**(26), 30275–30281 (2016).
9. B. Meng et al., "Coherent emission from integrated Talbot-cavity quantum cascade lasers," *Opt. Express* **25**(4), 3077–3082 (2017).
10. A. A. Golubentsev, V. V. Likhanskiĭ, and A. P. Napartovich, "Theory of phase locking of an array of lasers," *Sov. Phys. JETP* **66**(4), 676–682 (1987).
11. D. Mehuys et al., "Modal analysis of linear Talbot-cavity semiconductor lasers," *Opt. Lett.* **16**(11), 823–825 (1991).
12. F.-L. Yan et al., "High-power phase-locked quantum cascade laser array emitting at $\lambda \sim 4.6$ μm," *AIP Adv.* **6**(3), 35022 (2016).
13. D. Botez, "Monolithic phase-locked semiconductor laser arrays," in *Diode Laser Arrays*, pp. 1–72, Cambridge University Press, New York (1994).
14. C. Zmudzinski et al., "Coherent 1 W continuous wave operation of large-aperture resonant arrays of antiguided diode lasers," *Appl. Phys. Lett.* **62**(23), 2914–2916 (1993).
15. H. Yang et al., "10 W near-diffraction-limited peak pulsed power from Al-free, 0.98um-emitting phase-locked antiguided arrays," *Electron. Lett.* **33**(2), 136–137 (1997).
16. H. Yang, L. J. Mawst, and D. Botez, "1.6 W continuous-wave coherent power from large-index-step ($\Delta n \approx 0.1$) near-resonant, antiguided diode laser arrays," *Appl. Phys. Lett.* **76**(10), 1219–1221 (2000).
17. C. A. Zmudzinski, D. Botez, and L. J. Mawst, "Simple description of laterally resonant, distributed-feedback-like modes of arrays of antiguides," *Appl. Phys. Lett.* **60**(9), 1049–1051 (1992).
18. A. Bismuto et al., "Large cavity quantum cascade lasers with InP interstacks," *Appl. Phys. Lett.* **93**, 231104 (2008).
19. C. Sigler et al., "4.7 μm-emitting near-resonant leaky-wave-coupled quantum cascade laser phase-locked arrays," *IEEE J. Sel. Top. Quantum Electron.* **23**(6), 1200706 (2017).
20. T. S. Mansuripur et al., "Single-mode instability in standing-wave lasers: the quantum cascade laser as a self-pumped parametric oscillator," *Phys. Rev. A* **94**(6), 63807 (2016).
21. M. Brandstetter et al., "Spectrally resolved far-fields of terahertz quantum cascade lasers," *Opt. Express* **24**(22), 25462–25470 (2016).
22. C. Sigler et al., "Design of resonant leaky-wave coupled phase-locked arrays of mid-IR quantum cascade lasers," *IEEE J. Sel. Top. Quantum Electron.* **21**(6), 97–106 (2015).
23. D. Botez et al., "Resonant optical transmission and coupling in phase-locked diode laser arrays of antiguides: the resonant optical waveguide array," *Appl. Phys. Lett.* **54**(22), 2183–2185 (1989).
24. D. Botez, L. J. Mawst, and G. Peterson, "Resonant leaky-wave coupling in linear arrays of antiguides," *Electron. Lett.* **24**(21), 1328 (1988).
25. P. Yeh, D. Botez, and C. Gu, "Optical properties of dual-state Fabry–Perot étalons," *Opt. Lett.* **17**(24), 1818–1820 (1992).
26. Y. Bai et al., "Room temperature continuous wave operation of quantum cascade lasers with watt-level optical power," *Appl. Phys. Lett.* **92**, 101105 (2008).
27. D. Botez et al., "Phase-locked arrays of antiguides: modal content and discrimination," *IEEE J. Quantum Electron.* **26**(3), 482–495 (1990).
28. L. J. Mawst et al., "High-power, in-phase-mode operation from resonant phase-locked arrays of antiguided diode lasers," *Appl. Phys. Lett.* **55**(1), 10–12 (1989).

Chris Sigler received his BS degree in computer engineering from Michigan State University in 2012. He is currently working toward

a PhD in the Department of Electrical and Computer Engineering at the University of Wisconsin–Madison. His graduate studies have focused on the simulation and fabrication of quantum cascade lasers, particularly on high-power QCL phase-locked arrays, and grating-coupled surface-emitting QCLs.

Ricky Gibson received his BS degree in physics from California Polytechnic State University in 2006, his MS degree in physics from California State University, Fullerton, in 2008, and his MS and PhD degree in optical sciences from University of Arizona in 2011 and 2016. He is currently a research scientist with University of Dayton Research Institute/Air Force Research Laboratory. Recent research areas have included plasmonics, photonic crystals, III-V molecular beam epitaxy, and semiconductor lasers.

Colin Boyle received his BS degree in physics from Miami University, Oxford, Ohio, in 2009. He is currently working toward his PhD in the Department of Electrical and Computer Engineering at the University of Wisconsin–Madison. His graduate studies have focused on the fabrication and design of quantum cascade lasers, particularly of grating-coupled surface-emitting QCLs and phase-locked QCL arrays.

Jeremy D. Kirch received his BS degree in electrical engineering and physics from the University of Wisconsin–Madison in 2007, where he is currently working toward his PhD in the Department of Electrical and Computer Engineering, as a Roger Bacon Fellowship recipient. His graduate studies have consisted of investigations into compressively strained metamorphic buffer layers grown by MOCVD for use with type-I QW lasers, and QCL design, fabrication, and testing, including research into high-power QCL phase-locked arrays.

Donald Lindberg III received his BS degree in electrical engineering from the University of Wisconsin—Madison in 2000. He began his career at diode-laser manufacturer Alfalight, Inc., where he fabricated R&D test and measurement systems. Later, he performed epitaxial growth via MOCVD. Currently, he is an industrial consultant for Intraband, LLC, where he is an R&D test and measurement engineer, focusing on high-power QCL development. Furthermore, he is a facilities technician at Compound Photonics.

Thomas Earles received his BS and MS degrees in electrical engineering. In 1999, he left graduate school to cofound a diode laser manufacturing company, Alfalight Inc. He is currently the director of product development for Intraband, LLC, which is developing high-power quantum cascade lasers.

Dan Botez received his BS, MS, and PhD degrees in electrical engineering from the University of California–Berkeley in 1971, 1972, and 1976, respectively. He is currently the Philip Dunham Reed Professor of electrical engineering at the University of Wisconsin–Madison. His current research interests lie in three areas of semiconductor-laser device physics: quantum cascade lasers; high-power, coherent edge-emitting lasers; and high-power, coherent grating-coupled surface-emitting lasers. He has authored or coauthored more than 450 technical publications of which over 340 were refereed, and holds 56 patents. He is a fellow of the IEEE and the OSA.

Luke J. Mawst received his BS degree in engineering physics and his MS and PhD degrees in electrical engineering from the University of Illinois at Urbana–Champaign in 1982, 1984, and 1987, respectively. He is currently a professor in the electrical and computer engineering department at the University of Wisconsin–Madison, where he is involved in the development novel III/V compound semiconductor device structures, including quantum cascade lasers, leaky-mode photonic crystal lasers, and high-power diode lasers. He has authored or coauthored more than 250 technical journal articles and holds 26 patents. He is a fellow of IEEE and member of OSA.

Robert Bedford received his PhD from the University of Arizona in 2003 before joining the technical staff of the optoelectronic technology branch within the sensors directorate, Air Force Research Laboratory. He is additionally an adjunct professor at the College of Optical Sciences at UA. Current research areas including high-brightness semiconductor lasers operating in the short- and mid-wave infrared spectrum, and energetic pulsed semiconductor lasers. He is a senior member of both IEEE and OSA.